MODIS/ASTER (MASTER) Airborne simulator

Level 3 Elevated Temperature Features (ETF) and Fire Radiative Power (FRP) Algorithm Theoretical Basis Document (ATBD)

Version 0.1
November 20, 2025

[1]Federico Rabuffi, [1,2]Michael S. Ramsey, [3]James O. Thompson, [1]Glynn Hulley, [1]Simon J. Hook

MASTER Algorithm Development Team

[1]NASA-Jet Propulsion Laboratory, California Institute of Technology
[2]University of Pittsburgh
[3]University of Texas, Austin

National Aeronautics and Space Administration
Jet Propulsion Laboratory
California Institute of Technology

Jet Propulsion Laboratory
4800 Oak Grove Drive
Pasadena, California 91109-8099
California Institute of Technology

This research was carried out at the Jet Propulsion Laboratory, California Institute of Technology, under a contract with the National Aeronautics and Space Administration.

Change History Log

Revision	Effective Date	Prepared by	Description of Changes
Draft	20/11/2025	Federico Rabuffi	First draft

1 Contacts

Readers seeking additional information about this study may contact the following:

Federico Rabuffi
NASA – Jet Propulsion Laboratory, California Institute of Technology
4800 Oak Grove Drive, Room 183-5906B
Pasadena, California 91109-8099
Email: federico.rabuffi@jpl.nasa.gov
Office: 1-818-354-0854

Michael S. Ramsey
University of Pittsburgh
4107 O'Hara Street, Room 509
Pittsburgh, PA 15260-3332
Email: mramsey@pitt.edu
Office: 1-412-624-8772

James O. Thompson
University of Texas, Austin
10611 Exploration Way
Austin, TX 78758
Email: james.thompson@beg.utexas.edu
Office: 1-512-471-6775

Glynn Hulley
NASA – Jet Propulsion Laboratory, California Institute of Technology
4800 Oak Grove Drive
Pasadena, California 91109-8099
Email: glynn.hulley@jpl.nasa.gov
Office: 1-818-354-2979

Simon J. Hook
NASA – Jet Propulsion Laboratory, California Institute of Technology
4800 Oak Grove Drive
Pasadena, California 91109-8099
Email: simon.j.hook@jpl.nasa.gov
Office: 1-818-354-0974

2 Abstract

The MODIS/ASTER Airborne Simulator was developed for the Advanced Spaceborne Thermal Emission and Reflection Radiometer (ASTER) and Moderate Resolution Imaging Spectroradiometer (MODIS) projects. ASTER and MODIS are two spaceborne imagining instruments launched in the fall of 1999 hosted on Terra platform. ASTER provides high spatial resolution observations with 15 m in the VNIR, 30 m in the SWIR and 90 m in the TIR across a total of 14 spectral channels, spanning approximately 0.5 to 12 micron. The swath is 60 km, and it achieves nominal 16 day repeat coverage. ASTER has also along-track stereo imaging, enabling detailed topographic and local-scale studies using visible through thermal infrared data.

MODIS provides moderate-to-coarse resolution observations of 250 m (2 channels), 500 m (5 channels) and 1 km (29 channels) covering a spectral range from 0.4 to 14 micron. Its swath width is 2330 km, providing near-daily global coverage (with the except near the equator).

The primary mission of MASTER was to collect ASTER-like and MODIS-like data, at higher spatial resolution, to provide an additional radiometric calibration and to support validation of the ASTER and MODIS geophysical retrieval algorithms and permit scaling studies and comparison with in-situ measurements.

Beyond his primary objectives, over the years, MASTER has continued to operate, evolving into the Geological Earth Mapping Experiment (GEMx) – a joint campaign between NASA and the U.S. Geological Survey (USGS). GEMx is designed to map portions of the southwest United States for critical minerals using advanced airborne imaging. In addition to that, MASTER serves as a key platform for generating simulated data in support of future thermal infrared missions, as the Surface Biology and Geology – Thermal Infrared (SBG-TIR), Thermal Infrared Imaging Satellite for High-resolution Natural resource Assessment (TRISHNA), Landsat Next, and Land Surface Temperature Monitoring (LSTM).

This document describes the Level-3 Elevated Temperature Features (ETF) and Fire Radiative Power (FRP) products.

Contents

Figures

Tables

3 Introduction

The MODIS/ASTER (MASTER) airborne simulator is a multispectral scanning instrument that acquires data across the 0.4-to-13-micron spectral window using 50 channels spanning in visible (VIS), near infrared (NIR), shortwave infrared (SWIR), mid infrared (MIR) and thermal infrared (TIR). Depending on the aircraft altitude, the spatial resolution provided by MASTER can vary between approximately 5 to 50 m, with an 85.9° total field of view and a variable swath width determined by the aircraft platform (DOE B200, NASA ER-2, or NASA DC-8). A comparison with spaceborne thermal sensors in orbit and planned, is reported in Table 1.

Table 1: MASTER measurement characteristics compared to other operational and planned (*) spaceborne TIR instruments

Instrument	**Platform**	**Resolution (m)**	**Revisit (days)**	**Daytime overpass**	**TIR bands (8-12.5 µm)**	**Launch year**
MASTER	**Aircraft: B200; ER-2; DC-8**	**~ 5 to 50 (altitude dependent)**	**Airborne campaign-based**	**Yes – campaign based**	**10**	**1st campaign 1998-1999**
OTTER	SBG	60	3	12:30	6	2028*
ECOSTRESS	ISS	38 × 68	3-5	Variable	5	2018
LSTM		50	4	13:00	5	2028*
TRISHNA		57	2-3	13:00	4	2025*
ASTER	Terra	90	16	10:30	5	1999
ETM+/TIRS	Landsat 7/8	60-100	16	10:11	1/2	1999/2013
VIIRS	Suomi-NPP	750	Daily	1:30 / 13:30	4	2011
MODIS	Terra/Aqua	1000	Daily	10:30 / 13:30	3	1999/2002
GOES	Multiple	4000	Daily	Every 15 min	2	2000

This document outlines the theory and methodology for generating the MASTER Level-3 (L3) Elevated Temperature Features (ETF) and Fire Radiative Power (FRP) products. The MASTER L3 ETF product uses the MASTER Level – 1B (L1B) MIR and TIR calibrated radiance. High temperature surface targets such as volcanic eruptions, wildfires, and certain anthropogenic infrastructure results in elevated MIR and TIR radiance. The initial detection and continual monitoring of these features, commonly referred to as "thermal anomalies" are critical for hazard assessment (e.g., new volcanic activity, wildfire movement) and certain anthropogenic outputs (e.g., hydrocarbon gas flaring and stack temperatures). Early studies using TIR data simply describe the detection of a new thermal anomaly at a quiescent volcano. Ramsey and Harris (2013) summarized the history of satellite-based TIR research of active volcanoes into four broad themes: (1) thermal detection, (2) analysis of sub-pixel components, (3) heat/mass flux studies, and (4) eruption chronologies.

More recently, the number, size, and severity of wildfires have increased dramatically with a changing climate, resulting in increased infrastructure damage and decreased air quality (Wooster et al., 2003; Vasileva and Moiseenko, 2013; Jaffe et al., 2020). Multispectral MIR and TIR data of an entire wildfire can aid in active fire detection, movement over time, and plume characterization, all of which are vital for fire managers if the information is provided rapidly.

MASTER is sensitive to a large range of temperatures thereby enabling detection of most thermal anomalies on Earth without detector saturation (Table 2). The maximum radiometric emission for the typical range of Earth surface temperatures (~ 200 to 330 K) is found in the thermal infrared region (8 – 13 μm), which shifts to the MIR region (3.5 – 5 μm) for elevated temperature features (> 500 K). The emitted energy in these windows for a given wavelength is a function of both temperature and emissivity. Because the ETF product assumes blackbody

emission (emissivity, $\varepsilon = 1.0$), derived temperatures could have larger uncertainties for surfaces with an $\varepsilon < 1.0$.

ETF is applied to the MIR and TIR L1B surface radiance data for the entire land surface imaged by MASTER. Any pixel identified as having an elevated temperature by the algorithm is flagged in the ETF and used to produce FRP.

The remainder of the document discusses the MASTER instrument characteristics, provides background on TIR remote sensing, presents the testing approach for the numerous algorithms considered, gives a full description and background on the chosen ETF and FRP algorithms.

4 MASTER - Instrument Characteristics

4.1 Radiometer

As described in Hook et al., (2001) - The MASTER instrument was developed by the NASA Ames Research Center in conjunction with the Jet Propulsion Laboratory. It consists of three key components: a scanning spectrometer, a digitizer, and a data storage system. The scanning unit was built by Sensys Technology (formerly Daedalus Enterprises), while the digitizer and data storage system was a collaborative effort between Berkeley Camera Engineering and the Ames Airborne Sensor Facility (ASF), which also managed the system integration.

MASTER supports a variety of scan speeds, allowing the acquisition of contiguous imagery from different altitudes and with varying pixel sizes (Table 2). The optical system includes a spectrometer mounted on a scanning fore-optic unit. Both the spectrometer and fore-optics portions are mated to an optical baseplate. The fore-optics employ a 45° rotating scan mirror that directs light into a Gregorian telescope, through a series of mirrors and apertures, and finally into

the spectrometer.

The spectrometer separates incoming radiation into four wavelength regions – VIR, SWIR, MIR and TIR – using dichroic beam slitters. Each region is dispersed by a diffraction grating onto its own detector array. The system design ensures high optical efficiency and radiometric uniformity across the field of view. Electrical signals from the detectors are amplified, digitized through adaptive 16-bit converters, and stored along with navigation and engineering data. The use of actively controlled preamplifiers and optical isolation minimizes noise and calibration drift, ensuring high radiometric accuracy. Further details of the optical system are given in King et al. (1996).

Table 2: MASTER sensor - Summary Characteristics

Summary characteristics	
Wavelength Range (µm)	0.4 - 13
Number of channels	50
Number of pixels	716
Instantaneous field of view	85.92°
Platforms	DOE King Air Beachcraft B200; NASA ER-2; NASA DC-8
Pixel size DC-8 (m)	10 – 30
Pixel size NASA ER-2 (m)	50
Pixel size DOE King Air Beachcraft B200 (m)	5 – 25
DC-8 range – without refueling	5403 statute miles
ER-2 range – without refueling	3700 statute miles
B200 range – without refueling	700 statute miles
Scan speed	6.25/12/5/25 rps
Calibration VIS-SWIR	Laboratory Integrating Sphere
Calibration MIR-TIR	2 on-board blackbodies
Data Format	Hierarchical Data Format (HDF)
Digitalization	16-bit
Products	
Level 1B	Radiance at sensor
Level 2	Emissivity and Land Surface Temperature
Level 3	Surface Mineralogy Analysis
	Evapotranspiration
	Elevated Temperature Feature
	Fire Radiative Power

4.2 Band positions

MASTER - airborne sensor - acquires multispectral data across the VSWIR to TIR region using 50 channels ranging from 0.4 to 13 microns. The spectral configuration, listed in Table 3, is divided into 4 regions: VNIR (channels 1-11); SWIR (channels 12-25); MIR (channels 26-40); TIR (channels: 41-50). The center wavelength position and width of each band – width-at-half-maximum (FWHM) – are defined by the geometry of the grating-based spectrometer and are calibrated before and after each major flight campaign. Therefore, small shift in channel center positions may occur between calibration cycles and the calibration closest to the acquisition date should be used when performing quantitative spectral analyses.

Table 3: MASTER SRF based on the 2025 campaign - Date of Calibration: Sep 2025; location: NASA Aims. More details at: https://asapdata.arc.nasa.gov/sensors/master/data/srf/Sep_25_srf.html

(μm)	Band#	Full width half maximum	Channel Center	Channel peak
VNIR – 1	1	0.0412	0.4596	0.46
VNIR – 2	2	0.0451	0.4984	0.5
VNIR – 3	3	0.0431	0.5409	0.542
VNIR – 4	4	0.0412	0.5804	0.58
VNIR – 5	5	0.0598	0.6602	0.652
VNIR – 6	6	0.0412	0.7101	0.71
VNIR – 7	7	0.0405	0.7495	0.75
VNIR – 8	8	0.0406	0.7991	0.8
VNIR – 9	9	0.0412	0.8651	0.866
VNIR – 10	10	0.0408	0.9053	0.906

VNIR – 11	11	0.0418	0.946	0.946
SWIR – 1	12	0.056	1.6037	1.604
SWIR – 2	13	0.055	1.6605	1.66
SWIR – 3	14	0.0516	1.7153	1.716
SWIR – 4	15	0.0526	1.7696	1.77
SWIR – 5	16	0.0479	1.8249	1.83
SWIR – 6	17	0.04	1.8744	1.876
SWIR – 7	18	0.0504	1.927	1.928
SWIR – 8	19	0.0476	1.9764	1.978
SWIR – 9	20	0.0479	2.0787	2.08
SWIR – 10	21	0.0468	2.1605	2.162
SWIR – 11	22	0.0485	2.2107	2.212
SWIR – 12	23	0.0473	2.2604	2.262
SWIR – 13	24	0.0701	2.3298	2.32
SWIR – 14	25	0.0632	2.3961	2.39
MIR – 1	26	0.1457	4.0552	4.065
MIR – 2	27	0.144	3.2864	3.295
MIR – 3	28	0.1486	3.4405	3.455
MIR – 4	29	0.1479	3.5966	3.61
MIR – 5	30	0.135	3.7432	3.76
MIR – 6	31	0.1534	3.9009	3.915

MIR – 7	32	0.1457	4.0552	4.065
MIR – 8	33	0.153	4.2472	4.2426
MIR – 9	34	0.153	4.3812	4.3766
MIR – 10	35	0.1412	4.5119	4.52
MIR – 11	36	0.1481	4.6633	4.68
MIR – 12	37	0.1477	4.8149	4.83
MIR – 13	38	0.1402	4.9601	4.98
MIR – 14	39	0.1434	5.1038	5.105
MIR – 15	40	0.1376	5.2518	5.26
TIR – 1	41	0.2805	7.8069	7.83
TIR – 2	42	0.4333	8.1814	8.25
TIR – 3	43	0.3683	8.6155	8.65
TIR – 4	44	0.3837	9.0527	9.05
TIR – 5	45	0.377	9.6853	9.71
TIR – 6	46	0.3745	10.0892	10.11
TIR – 7	47	0.6101	10.6241	10.58
TIR – 8	48	0.6973	11.3144	11.17
TIR – 9	49	0.4929	12.1104	12.06
TIR – 10	50	0.4754	12.8487	12.81

4.3 Comparison with SBG-TIR (Surface Biology and Geology – Thermal Infrared)

This section presents a spectral comparison between SBG-TIR and MASTER to analyze their level of compatibility for ETF and FRP applications. This includes the study of band positions, widths and overall spectral coverage. This comparative analysis allows assessment of how closely the two sensors align, supporting the reliability of transferring the methodology and validation procedures developed for SBG-TIR to MASTER (Figure 1).

The spectral comparison between SBG-TIR and MASTER reveals a high degree of correspondence in band positioning within the MIR and TIR regions. In the MIR region, MASTER bands 31 and 37 show excellent alignment with SBG MIR-1 and MIR-2 The two sensors share the same six-band configuration covering the 8-12 µm atmospheric window. MASTER bands 42-44 and 46-49 align closely with SBG-TIR channels: band 42 (center: 8.18 µm) corresponds to TIR-1 (8.32 µm) with a deviation of 0.14 µm; band 43 (8.62 µm) matches TIR-2 (8.63 µm) within 0.01 µm; band 44 (9.05 µm) aligns with TIR-3 (9.07 µm) with 0.02 µm difference; band 46 (10.08 µm) relates to TIR-4 (10.30 µm) showing the largest offset of 0.22 µm; band 48 (11.31 µm) corresponds to TIR-5 (11.35 µm) with 0.04 µm deviation; and band 49 (12.11 µm) aligns with TIR-6 (12.05 µm) within 0.06 µm.

Overall, despite some small variation, the sensors can be considered spectrally comparable with respect to the algorithm's applicability to ETF and FRP applications.

Nevertheless, MASTER data were in fact chosen to simulate SBG-TIR data not only for ETF and FRP, but also for mineralogical applications (Ramsey et al., 2024, Ramsey et al., 2025, Rabuffi et al., 2025).

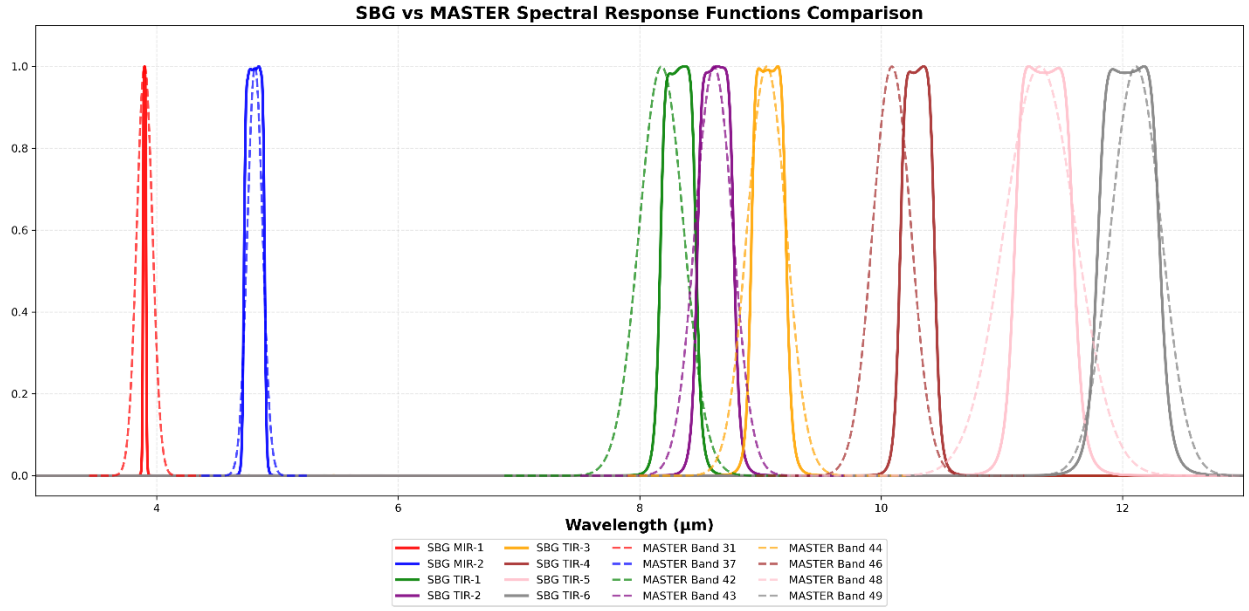

Figure 1: Spectral comparison between the SBG and MASTER sensors.

5 Theory

5.1 Mid-wave and Thermal Infrared Remote Sensing Background

The at-sensor measured radiance in the infrared region (3–13 μm) consists of a combination of different terms from surface emission, solar reflection, and atmospheric emission and attenuation. The Earth-emitted radiance is a function of the temperature and emissivity of the surface, which is then attenuated by the atmosphere on its path to the satellite. The emissivity of an isothermal, homogeneous emitter is defined as the ratio of the actual emitted radiance to the radiance emitted from a blackbody at the same thermodynamic temperature (Norman and Becker 1995), $\epsilon_\lambda = R_\lambda / B_\lambda$. Emissivity is an intrinsic property of the surface material and is an independent measurement from the surface temperature, which varies with irradiance, local atmospheric conditions, time of day, and specific conditions causing elevated temperature (e.g., wildfires, volcanic eruptions, etc.). The emissivity of most natural Earth surfaces varies from ~0.7 to close to 1.0, for the TIR wavelength (8–13 μm) for spatial scales <100 m. Narrowband emissivities less than 0.85 are typical for most desert and semi-arid areas due to the strong quartz absorption feature (Reststrahlen band) between the 8.0 and 9.5 μm, whereas the emissivity of green vegetation and water are generally greater than 0.95 and spectrally flat in the TIR. Dry and senesced vegetation as well as ice and snow can have lower emissivity values in the wavelengths longer than 10 μm.

The atmosphere also emits TIR radiation, a percentage of which reaches the sensor directly as "path radiance," whereas some amount is radiated downward to the surface (irradiance) and reflected back to the sensor. This is commonly known as the reflected downwelling sky irradiance. One effect of the sky irradiance is the reduction of the spectral contrast of the emitted surface radiance, due to Kirchhoff's law. Assuming the spectral variation in emissivity is small (Lambertian assumption) and using Kirchhoff's law to express the hemispherical-directional

reflectance as directional emissivity (ρ_λ=1-ϵ_λ), the at-sensor measured radiance in the infrared spectral region is a combination of three primary terms: the Earth-emitted radiance, reflected downwelling radiance (thermal + solar components), and total atmospheric path radiance (thermal + solar components).

$$L_{obs}(\lambda,\theta) = \tau_\lambda(\theta)\left[\epsilon_\lambda B(\lambda,T_s) + \rho_\lambda\left(L_s^{\downarrow}(\lambda,\theta) + L_t^{\downarrow}(\lambda,\theta)\right)\right] + L_t^{\uparrow}(\lambda,\theta) + +L_s^{\uparrow}(\lambda,\theta) \quad (1)$$

where: L(λ,θ) = at-sensor radiance, λ is wavelength, θ is the satellite viewing angle, ϵ_λ is the surface emissivity, ρ_λ is surface reflectance, B(λ,T_s) is the Planck function describing radiance emitted at surface temperature, T_s, $L_s^{\downarrow}$ is the total (diffuse and direct) downwelling solar radiance, $L_t^{\downarrow}$ is the downwelling thermal irradiance, τλ (θ) is the atmospheric transmittance, Ls↑ (λ,θ) is the upward path solar radiance, and Lt↑ (λ,θ) is the upward thermal path radiance reaching the sensor.

Reflected solar radiation in the mid-wave infrared region is non-negligible for highly reflective surfaces, whereas the same term in the thermal infrared region is generally smaller in magnitude (~10%) than the surface-emitted radiance particularly over highly reflective surfaces and on humid days where atmospheric water vapor content is high. This contribution in both IR regions needs to be taken into account in the atmospheric correction process. However, for high temperature surfaces, the emitted radiance (varying by T^4) dominates all atmospheric terms, which are typically ignored using the radiance-at-sensor values for all calculations. As stated in the SBG-TIR ETF ATBD documentation, these temperatures are calculated using a simple temperature-emissivity approach that assumes an ε = 1.0 at one of the infrared wavelengths and solving the Plank Equation for the emitted surface temperature.

5.2 Infrared Thermal Anomaly Detection

Remote sensed data have been used to detect and monitor volcanic eruptions and wildfires from the earliest days of the satellite era (e.g., Gawarecki et al., 1965; Williams and Friedman, 1970; Scorer, 1986). These studies focused mostly on hot spot detection and temperature measurements using TIR data. They became ever more complex with the launch of new sensors providing better spatial, temporal, and spectral data. For example, the ability to extract critical information from the subtle phases of precursory activity to the detailed spectral mapping of the erupted products grew exponentially (Ramsey and Harris, 2013).

The ever increasing amount of orbital data has resulted in a wide range of temporal and spatial scales with a large number of algorithms designed to automatically detect pixels that are deemed “thermally anomalous”. These detection algorithms are commonly rooted in analysis of the spatial, spectral, and/or temporal (or some combination thereof) scales of the data. For example, an algorithm may use the change in temperature of a region over time to identify the appearance of a thermal anomaly (e.g., Tramutoli et al. 1998), whereas other approaches determine the radiance difference between bands (e.g., Wright et al., 2002), or that spectral changes over a spatial area (Coppola et al., 2016a) to identify an elevated temperature feature.

Whether a thermal anomaly detection algorithm operates by assessing radiance (or temperature) in spectral, spatial, or temporal space, the methods can be divided into four categories: fixed threshold, contextual, temporal, or hybrid. Fixed threshold algorithms are spectrally based and use data for a single pixel to assess whether the radiance (or temperature) in the MIR and/or TIR bands is thermally anomalous. In contrast, contextual algorithms use the difference between a pixel’s radiance (or temperature) and that of its surrounding pixels (e.g., “the background temperature”) to assess its state. Temporal algorithms operate by comparing a pixel’s

radiance (or temperature) with the preceding historical values for the same pixel over time. These time series allow typical pixel values for any given time of day and year to be defined, and divergences from the baseline to be statistically assessed. However, by definition, they rely on prior data and become more appropriate as more data becomes available. More recent algorithms have incorporated aspects of one or more of these three categories and are dubbed hybrid approaches. Many of these algorithms are now benefiting from the application of Artificial Intelligence (AI) models to improve these prior statistical approaches (Amato et al., 2023; Corradino et al., 2022; Corradino et al., 2023; Piscini and Lombardo, 2014).

Regardless of the general approach to identifying thermally elevated pixels in an infrared image, every algorithm aims to detect the greatest number of true thermal anomalies by minimizing errors related to false positives. This goal is crucial to perform operationally over a global scale under widely varying conditions.

The studies performed for SBG-TIR, and illustrated in the relative ATBD (https://sbg.jpl.nasa.gov/doc_links), carried out a comprehensive evaluation of the hotspot-detection algorithm following the validation strategies established in previous infrared anomaly studies. A ground truth dataset was generated through manual identification of true thermal anomalies, and the algorithm performance was assessed using three common approaches: qualitative comparison with reference rime series, image-level accuracy based on omission and commission errors, and pixel-level analysis using precision, recall, and F1-score. See SBG-TIR ETF ATBD for more information (https://github.com/sbg-tir/SBG-TIR-L3-ETF/tree/main/Documentation).

6 Elevated Temperature Feature (ETF) Algorithm

The algorithm selection process adopted for the SBG-TIR L3 ETF products is also considered valid for generating the MASTER L3 ETF product, as supported by the considerations presented in Section 4.3. Among the six different algorithms tested and evaluated, the selection process—which involved assessing multiple candidate approaches—ultimately led to a modified version of the MIROVA algorithm, chosen for its optimal balance between computational efficiency and robust performance metrics across a range of thermal anomaly types, including volcanoes and fires.

The changes in MIROVA algorithm include an enhanced Normalized Thermal Index (NTI), which in its final form will use one MIR band (around 4 μm) and two TIR bands (around 11.3 μm and 12 μm) (Shreevastava et al., 2023) operating on brightness temperature data with no dependences on external auxiliary files. Another critical change is the two-pass hybrid approach, that refines the detection process through a specific sequence of filter defined as “first-pass” and “second-pass”.

The two-pass hybrid approach is composed by the Normalized Thermal Index (NTI) thresholding step followed by the Enhanced Thermal Index (ETI). Shreevastava et al. (2023) demonstrated that combining an NTI threshold of −0.7 with an ETI threshold of 0.02 yields an ETF detection accuracy of approximately 97%, with sensor noise up to 0.5 K having negligible effects in the 400–1200 K temperature range.

6.1 Normalized Thermal Index (NTI)

The detection of elevated temperature features (ETF) relies on the differential response of the Planck function in the Mid-Infrared (MIR) and Thermal Infrared (TIR) spectral regions.

High-temperature sub-pixel features (e.g., >500 K) exhibit peak radiance in the MIR (3–5 μm), whereas background Earth surface temperatures (250–320 K) peak in the TIR (8–12 μm). The Normalized Thermal Index (NTI) exploits this spectral contrast to identify pixels containing thermal anomalies. The NTI is calculated as a normalized difference ratio between the at-sensor radiance observed in the MIR (L_{MIR}) and TIR (L_{TIR}) bands:

$$\frac{L_{MIR} - L_{TIR}}{L_{MIR} + L_{TIR}}$$

Sensitivity analyses performed for SBG-TIR indicated that the 4 μm MIR band minimizes false negatives for features above 400 K, making it preferable over the 4.8 μm band. This MIR band is paired with a TIR band at approximately 11.3 or 12 μm. As detailed in Section 4.3, this configuration is also valid for MASTER. To identify prominent hotspots, fixed thresholds are applied to the NTI: −0.8 for nighttime acquisitions and −0.6 for daytime acquisitions.

6.2 Enhanced Thermal Index (ETI)

The Enhanced Thermal Index (ETI) provides a second-pass filter to improve the detection of smaller, cooler sub-pixel features (e.g., ~9 m^2 at 500 K) that may not exceed the global NTI threshold. The ETI compares the observed NTI to a modeled background NTI (NTI_{bg}) derived from the expected spectral behavior of thermally homogeneous surfaces.

The ETI computation involves three steps: First, an apparent NTI is computed. This represents the theoretical NTI value the pixel would exhibit if it were thermally homogeneous at the temperature observed in the TIR band (the brightness temperature, T_{TIR}); Then a quadratic regression is used to predict the expected background (NTI_{bg}) from the apparent NTI; Finally, the ETI is defined as the residual difference between the observed NTI and the modeled background:

$$ETI = NTI_{observed} - NTI_{bg}$$

The ETI serves as a second-pass filter that effectively flattens the background noise, allowing for the detection of anomalies that deviate from the homogeneous trend.

An ETI threshold of 0.02 (Shreevastava et al., 2023) accurately identifies sub-pixel ETFs missed by the initial NTI filter, achieving an overall detection accuracy of about 97% when combined with the NTI filter.

7 Fire Radiative Power (FRP) Algorithm

Fire Radiative Power (FRP) quantifies the instantaneous rate of radiant energy emitted by a fire, representing the radiative fraction of its total heat release. Because FRP is linearly related to the rate of fuel consumption, it serves as a direct proxy for fire intensity. Unlike traditional methods that estimate emissions by multiplying burned areas by uncertain fuel load densities, FRP offers a more direct assessment; determining the instantaneous FRP allows scientists to estimate the combustion rate (kg/sec), while integrating these measurements over time yields the total Fire Radiative Energy (FRE), which is linearly related to the total biomass mass combusted.

FRP retrieval is made possible by the instrument's high saturation temperatures, which allow the sensor to measure intense heat without saturating the detector. The retrieval for MASTER data utilizes the Single Waveband Method, which estimates FRP using a single Mid-Infrared band (approx. 4 μm) based on a fourth-order power-law approximation of Planck's law. This single-band approach is particularly advantageous because it avoids the errors associated with multi-band spatial misregistration and the difficulty of characterizing background signals in the Thermal Infrared (TIR) bands, where weak fires may be indistinguishable from ambient terrestrial noise.

Three primary approaches will be discussed for retrieving Fire Radiative Power (FRP) from remote sensing data: The Bi-Spectral Method (Dozier Method), and the two Single Waveband Methods - one developed by Kaufman et al., (1996, 1998a and 1998b) used with MODIS, and MIR radiance method (Wooster et al., 2003). MASTER L3 FRP products are generated using the approach based on the Single Waveband because of the limitations of the Bi-Spectral Method.

7.1 Bi-Spectral Method (Dozier Method)

This approach, developed by Dozier (1981), uses data from two widely separated infrared channels—typically the Middle Infrared (MIR) and Thermal Infrared (TIR). It solves the fire's sub-pixel temperature (T_f) and fractional area (P_f) by assuming the fire is a target of uniform temperature superimposed on a uniform background. Once these two variables are retrieved, FRP is calculated using the adapted Stefan-Boltzmann law:

$$FRP_{TRUE} = \varepsilon\sigma \sum_{k=1}^{n} p_k T_k^4$$

where FRE TRUE = Fire Radiative Power (Wm-2), n = number of temperature components in the fire, s = Stefan-Boltzmann constant (5.67 x 10^{-8} J s^{-1} m^{-2} K^{-4}), ε = fire graybody emissivity, p_k = fractional area of kth surface thermal component within the field of view, and T_k = kinetic temperature of the kth thermal component (K).

This method is highly sensitive to spatial misregistration between the two spectral bands. Furthermore, for lower-resolution sensors, the fire signal in the TIR band is often very weak (barely distinguishable from the background noise), whereas the MIR signal is strong. This disparity makes the retrieval unstable and prone to large errors when the background radiance is not perfectly characterized.

7.2 MODIS Method (Single Waveband)

To overcome the noise and registration issues of the bi-spectral method, Kaufman et al. (1996, 1998a, 1998b) developed a method relying solely on the MIR spectral band. This method uses an empirical relationship derived specifically for the MODIS sensor. It relates FRP directly to the difference between the brightness temperature of the fire pixel and the background raised to the eighth power:

$$FRP_{MODIS} = 4.34\ 10^{-19}\left(T_{MIR}^{8} - T_{b,MIR}^{8}\right)$$

where T_{MIR} and $T_{b,MIR}$ are, respectively, the radiative brightness temperatures of the fire pixel and the neighbouring non fire background (K) recorded in the MODIS MIR channel.

7.3 MIR Radiance Method (Single Waveband)

This method, presented by Wooster et al. (2003), is a physics-based single-band approach designed to be generic rather than sensor-specific. It exploits the fact that for typical fire temperatures (600–1600 K), the Planck's Radiation law $B(\lambda, T)$, for wavelength in the MIR MIR atmospheric window (3.4 μm – 4.2 μm) is well approximated by a fourth order power lawand the temperatures predominating in active fires. The MIR emitted spectral radiance of a fire, $L_{f,MIR}$ can be approximated as:

$$L_{f,MIR} = \varepsilon_{f,MIR}\, B(\lambda, T) \approx \varepsilon_{f,MIR} a T^{4}$$

where $\varepsilon_{f,MIR}$ is the emissivity of the fire in the MIR spectral band, a is a constant with units W m^{-4} sr^{-1} m^{-1} K^{-4}. This power law reflects the Stefan-Boltzmann law (Radiative Power = $\varepsilon\sigma\ T^{4}$). Based on Plank's Radiation and Stefan-Boltzman laws, Wooster et al. (2003) show that the

radiative power of a subpixel fire is linearly proportional to the MIR radiance increase of the pixel above that of the ambient background:

$$FRP_{MIR} = \frac{A_{samp}\sigma}{a}(L_{h.MIR} - L_{bk,MIR})$$

where $L_{h.MIR}$ and $L_{bk,MIR}$ are the MIR radiances of the active fire and ambient background, respectively, A_{samp} is the pixel sampling area and a is a const

This method avoids the TIR noise issues of the bi-spectral method and the empirical limitations of the MODIS method and can be tuned to different by simply adjusting the constant.

Despite the many advantages some limitations rely on the validity of the power-law approximation.

8 MASTER Level-3 ETF and FRP outputs

The MASTER Level-3 ETF and FRP products are provided in .hdf5 format and include the following Scientific Data Sets (SDS). The ETF product contains three SDSs describing brightness temperature: the original Brightness_Temperature, a masked Brightness_Temperature, and a binary masked Brightness_Temperature. All ETF temperature datasets are stored as Float32 values in Kelvin. The FRP product includes the SDS Fire_Radiative_Power, stored as Float32 values in megawatts (MW).

Table 4: The Scientific Data Sets (SDSs) for the L3 MASTER ETF and FRP products

Product	SDS	Data type	Units	Valid Range	Scale Factor	Offset
ETF	*Brightness_Temperature*	Float32	Kelvin	n/a	n/a	n/a
ETF	*Brightness_Temperature_masked*	Float32	Kelvin	n/a	n/a	n/a
ETF	*Brightness_Temperature_masked_binary*	Float32	n/a	n/a	n/a	n/a
FRP	*Fire_Radiative_Power*	Float32	MW			

9 Acknowledgements

This research was performed at the Jet Propulsion Laboratory, California Institute of Technology, under contract with the National Aeronautics and Space Administration (NASA).
We are thankful for the support of the NASA Earth Science Directorate. Many thanks to the MASTER team and others at JPL for making this research possible. Thanks to Claudia Corradino for supporting the development of the ETF algorithm.

10 References

Amato, E., Corradino, C., Torrisi, F., and Del Negro, C. (2023). A Deep Convolutional Neural Network for Detecting Volcanic Thermal Anomalies from Satellite Images. Remote Sensing, 15(15), 3718.

Coppola, D., Laiolo, M., Cigolini, C., Delle Donne, D., Ripepe, M. (2016a). Enhanced volcanic hot-spot detection using MODIS IR data: results from the MIROVA system. Geological Society, London, Special Publications, 426(1), 181-205.

Corradino, C., Amato, E., Torrisi, F., Del Negro, C. (2022). Data-Driven Random Forest Models for Detecting Volcanic Hot Spots in Sentinel-2 MSI Images. Remote Sensing, 14(17), 4370.

Corradino, C., Ramsey, M.S., Pailot-Bonnétat, S., Harris, A.J., Del Negro, C. (2023). Detection of subtle thermal anomalies: Deep learning applied to the ASTER global volcano dataset. IEEE Transactions on Geoscience and Remote Sensing, 61, 1-15.

Dozier, J. (1981), A method for satellite identification of surface temperature fields of subpixel resolution, Remote Sens. Environ., 11, 221 – 229

Gawarecki, S.J., Lyon, R.J.P., Nordberg, W. (1965). Infrared spectral returns and imagery of the Earth from space and their application to geological problems: Scientific experiments for manned orbital flight. American Astronautical Society Science and Technology, 4, 13–133.

Hook, S. J. Myers, J. J., Thome, K. J., Fitzgerald, M. and A. B. Kahle (2001). The MODIS/ASTER airborne simulator (MASTER) - a new instrument for earth science studies. Remote Sensing of Environment, vol. 76, Issue 1, pp. 93-102

Jaffe, D.A., O'Neill, S.M., Larkin, N.K., Holder, A.L., Peterson, D.L., Halofsky, J.E., Rappold, A. G. (2020). Wildfire and prescribed burning impacts on air quality in the United States. Journal of the Air & Waste Management Association, 70(6), 583-615.

Kaufman, Y. J., C. Justice, L. Flynn, J. Kandall, E. Prins, D. E. Ward, P. Menzel, and A. Setzer (1998a), Monitoring global fires from EOS-MODIS, J. Geophys. Res., 103, 32,215 – 32,239.

Kaufman, Y. J., R. G. Kleidman, and M. D. King (1998b), SCAR-B fires in the tropics: Properties and their remote sensing from EOS-MODIS, J. Geophys. Res., 103, 31,955 – 31,969.

Kaufman, Y., L. Remer, R. Ottmar, D. Ward, L. Rong, R. Kleidman, R. Fraser, L. Flynn, D. McDougal, and G. Shelton (1996), Relationship between remotely sensed fire intensity and rate of emission of smoke: SCAR-C experiment, in Global Biomass Burning, edited by J. Levine, pp. 685 – 696, MIT Press, Cambridge, Mass.

King, M. D., Menzel, W. P., Grant, P. S., Myers, J. S., Arnold, G. T., Platnick, S. E., Gumley, L. E., Tsay, S. C., Moeller, C. C., Fitzgerald, M., Brown, K. S., & Osterwisch, F. G. (1996). Airborne scanning spectrometer for remote sensing of cloud, aerosol, water vapor and surface properties. Journal of Atmospheric and Oceanic Technology, 13, 777 ± 794.

Norman, J. M., & Becker, F. (1995). Terminology in thermal infrared remote sensing of natural surfaces. Agricultural and Forest Meteorology, 77(3-4), 153-166.

Piscini, A., Lombardo, V. (2014). Volcanic hot spot detection from optical multispectral remote sensing data using artificial neural networks. Geophysical Journal International, 196(3), 1525-1535.

Ramsey, M.S., Harris, A.J.L. (2013). Volcanology 2020: How Will Thermal Remote Sensing of Volcanic Surface Activity Evolve over the next Decade?. Journal of Volcanology and Geothermal Research, 249, 217–233. doi:10.1016/j.jvolgeores.2012.05.011.

Scorer, R.S. (1986). Etna: The Eruption of Christmas 1985 As Seen By Meteorological Satellite. Weather, 41, 378–384. doi:10.1002/j.1477-8696.1986.tb03773.x.

Shreevastava, A., Hulley, G., & Thompson, J. (2023). Algorithms for Detecting Sub-Pixel Elevated Temperature Features for the NASA Surface Biology and Geology (SBG) Designated Observable. Journal of Geophysical Research: Biogeosciences, 128(7), e2022JG007370.

Tramutoli, V. (1998). Robust AVHRR Techniques (RAT) for Environmental Monitoring: theory and applications. In: Cecchi GZ E (ed) EUROPTO Conference on Remote Sensing of Geology, Land Management and Cultural Heritage III. SPEI, Barcelona, Spain, pp 101–113.

Vasileva, A., Moiseenko, K. (2013). Methane emissions from 2000 to 2011 wildfires in Northeast Eurasia estimated with MODIS burned area data. Atmospheric Environment, 71, 115-121.

Williams, R.S., Jr., Friedman, J.D. (1970). Satellite Observation of Effusive Volcanism. Journal of the British Interplanetary Society, 23, 441–450.

Wooster, M.J., Zhukov, B., Oertel, D. (2003). Fire radiative energy for quantitative study of biomass burning: Derivation from the BIRD experimental satellite and comparison to MODIS fire products. Remote Sensing of Environment, 86(1), 83-107.

Wright, R., Flynn, L., Garbeil, H., Harris, A., Pilger, E. (2002). Automated volcanic eruption detection using MODIS. Remote Sensing of the Environment, 82(1), 135-155.